Band Engineering through Pb-doping of Nanocrystal Building Blocks to Enhance Thermoelectric Performance in Cu_3SbSe_4

Shanhong Wan, Shanshan Xiao, Mingquan Li, Xin Wang, Khak Ho Lim, Min Hong, Maria Ibáñez, Andreu Cabot, Yu Liu**

Dr. S. Wan, S. Xiao, M. Li, Prof. Y. Liu

Anhui Province Key Laboratory of Advanced Catalytic Materials and Reaction Engineering
School of Chemistry and Chemical Engineering
Hefei University of Technology, 230009 Hefei, P.R. China
E-mail: yliu@hfut.edu.cn

X. Wang
Center of Analysis and Test
Jiangsu University, 212013 Zhenjiang, P.R. China.

Prof. K. H. Lim
Institute of Zhejiang University-Quzhou, 99 Zheda Rd.
324000 Quzhou, P.R. China.

Prof. M. Hong
Centre for Future Materials, and School of Engineering
University of Southern Queensland, 4300 Springfield Central Queensland Australia.
E-mail: min.hong@usq.edu.au

Prof. M. Ibáñez
IST Austria, Am Campus 1,
3400 Klosterneuburg, Austria.

Prof. A. Cabot
Catalonia Institute for Energy Research-IREC, Sant Adrià de Besòs, 08930 Barcelona, Spain.
Institució Catalana de Recerca i Estudis Avançats - ICREA, 08010 Barcelona, Spain.

Keywords: Cu_3SbSe_4 nanocrystal, solution processing, Pb doping, band engineering, thermoelectricity

Abstract: Developing cost-effective and high-performance thermoelectric (TE) materials to assemble efficient TE devices presents a multitude of challenges and opportunities. Cu_3SbSe_4 is a promising *p*-type TE material based on relatively abundant elements. However, its main challenge lies in its poor electrical transport properties. In this study, we develop an efficient and scalable solution-based approach to synthesize high-quality Cu_3SbSe_4 nanocrystals (NCs) doped with Pb at the Sb site. Subsequently, after ligand displacement and annealing treatments, the dried powders are consolidated into dense pellets, and their electrical and thermal transport properties are investigated. The results reveal that Pb doping effectively increases the charge carrier concentration, resulting in a significant increase in electrical conductivity, while the Seebeck coefficients remain consistently high. The calculated band structure shows that Pb doping induces band convergence, thereby increasing the effective mass. Furthermore, the large ionic radius of Pb^{2+} results in the generation of additional point and plane defects and interphases, dramatically enhancing phonon scattering, which significantly decreases the lattice thermal conductivity at high temperatures. Overall, a maximum figure of merit zT_{max}~0.85 at 653 K is obtained in $Cu_3Sb_{0.97}Pb_{0.03}Se_4$. This represents a 1.6-fold increase compared to the undoped sample and exceeds most doped Cu_3SbSe_4-based materials produced by solid-state, with additional advantages in terms of versatility and cost-effectiveness associated with the use of a solution-based technology.

1. Introduction

Thermoelectricity stands as a pivotal green energy conversion technology that allows for direct and reversible conversion of thermal and electric energy.[1,2] However, the low conversion efficiency and high cost have impeded the widespread commercialization of thermoelectric (TE) energy conversion systems beyond some niche markets.[3,4] The main challenge in the TE field is the development of cost-effective active materials that enable the assembly of high-performance TE devices. This endeavor holds the key to unlocking the full potential of future waste heat utilization, contributing significantly to environmental preservation, among other fields of application.[5–9]

The TE performance of a material is commonly evaluated using the dimensionless figure of merit zT, $zT=\sigma S^2T/\kappa_{tot}$, where σ represents electrical conductivity, S is the Seebeck coefficient, T denotes absolute temperature and κ_{tot} represents thermal conductivity.[1,5,10] These parameters are determined by the material's crystallographic and electronic structure, composition, and defects. The challenge lies in effectively decoupling these mutually coupled parameters to enhance performance. Optimizing charge transport performance relies on balancing carrier concentration (p), carrier mobility (μ) and effective mass (m^*), which can be accomplished by doping/alloying,[11–16] tuning the electronic band structure[6,17–19] and energy filtering effects,[20,21] among other strategies.[2,5,22] Minimizing the lattice thermal conductivity (κ_L) requires the construction of a multiscale hierarchical architecture to dampen acoustic sub-modes across all wavelength bands,[23,24] including nanoscale precipitates,[21,25] grain refinement,[20,26–28] dislocations,[29,30] point defects,[18,20,26] *etc.* Typically, a coordinated combination of several strategies is required to enhance TE performance, and the exploration of novel approaches to improve zT has remained a primary focus.

While some ternary and quaternary copper-based compounds have been extensively studied, I_3-V-VI_4 tetrahedrally coordinated semiconductors remain relatively unexplored in the context of energy conversion applications, *e.g.*, photovoltaics, photocatalysis, and

thermoelectricity.[31,32] Cu_3SbSe_4, based on relatively abundant and safe elements, features a diamond-like structure. It excels as a direct, narrow bandgap *p*-type semiconductor, characterized by its intricate crystal lattice and an electronic band structure characterized by significant degeneracy at the valence band maximum.[33] Importantly, the Cu-Se framework facilitates efficient hole transport, providing a high hole charge carrier mobility (μ_H), while simultaneously providing a reduced phonon mean free path.[32,34,35] These characteristics result in intrinsically low κ_{tot} and elevated *S*, rendering Cu_3SbSe_4 a promising candidate material for TE applications. Nonetheless, a significant limitation of Cu_3SbSe_4 is its insufficient free hole concentration, p_H, of *ca.* 10^{18} cm^{-3} at ambient temperatures, resulting in suboptimal σ.[36] Consequently, improvements in the TE performance of Cu_3SbSe_4 require increasing the p_H while simultaneously engineering its electronic band structure to maintain elevated *S* values.

First-principles calculations have revealed that the formation energy associated with doping at the Sb lattice sites is notably low, and the dopants in Sb site incorporation predominantly result in the formation of *p*-type semiconductors accompanied by the creation of Cu vacancies that increase p_H.[37,38] Consequently, it is customary to introduce heterovalent ions mainly at the Sb positions to finely modulate the p_H of Cu_3SbSe_4. Specifically, the substitution of pentavalent Sb ions by Ga,[39] In,[39] Ni,[40] Bi,[41] Ti,[42] and Al[39] ions has been employed to achieve p_H~10^{19} cm^{-3}, while doping with Sn[34,43] and Ge[44] increases p_H to more than 10^{20} cm^{-3}, thereby enhancing σ and contributing to the overall enhancement of the TE performance. Preliminary calculations indicate that Pb also serves as a favorable dopant for tuning the TE properties of Cu_3SbSe_4. However, reports on the use of Pb as a dopant on Cu_3SbSe_4 are very scarce. Previously, a microwave-assisted solvothermal method was used to prepare samples doped with 4% Pb, resulting in a TE performance of zT~0.52 at 623 K. The main mechanisms underlying this enhancement were related to i) Pb^{4+} acting as an acceptor dopant, optimizing p_H; and ii) the formation of PbSe secondary phase, reducing the thermal conductivity by the phonon scattering.[45]

However, a more thorough and detailed investigation is required. Pb is considered to be stable in the form of Pb^{2+} within the Cu_3SbSe_4 lattice. Thus, the substitution of the relatively small Sb^{5+} ions (0.6 Å) by a 2-fold larger Pb^{2+} (1.19 Å) is expected to induce significant lattice distortions, electronic structure modification, and lattice defects that have not been investigated. Additionally, adhering to the principles of green chemistry, we have utilized the minimal concentration of Pb required, ensuring compliance with safety standards for electronic materials.

In this study, we present a high-yield and scalable bottom-up approach to produce Cu_3SbSe_4 nanocrystals (NCs) with a controlled amount of Pb doping. The effect of Pb doping on the TE performance of hot-pressed Cu_3SbSe_4 nanomaterials is thoroughly explored and discussed. In detail, we first perform a detailed analysis of the valence states of Pb in the NCs and then investigate the effect of Pb doping on the electrical and thermal transport mechanisms of the Cu_3SbSe_4 matrix. Density functional theory (DFT) calculations are further performed to investigate the effect of Pb-doping on the band structure of Cu_3SbSe_4. As a result, the significantly enhanced zT is attributed to the valence band convergence effect caused by Pb doping in addition to an increase in p_H. These findings deepen our understanding of Pb doping's mechanisms in enhancing TE properties in this system, providing insights useful for future research, including the exploration of non-toxic dopants for medium-temperature applications.

2. Results and Discussion

Cu_3SbSe_4 NCs were synthesized by modestly scaling up the reaction volume from a previously established synthetic method.[41] In this method, the precursor of Se powder dissolved in OLA and DDT is injected into a preheated solution containing the cation mixture. **Figure 1**a displays a representative transmission electron microscopy (TEM) image of the synthesized quasi-spherical Cu_3SbSe_4 NCs, revealing their uniform size, with an average diameter of 19±3 nm. This synthetic approach yielded over 93%, enabling the production of approximately 3.0 g of NCs in a single batch.

The results of high-resolution TEM (HRTEM, Figure 1c) and X-ray diffraction (XRD) analysis (Figure 1d) elucidate the tetragonal crystal structure of Cu_3SbSe_4 with a space group of $I\bar{4}2m$ and determined lattice parameters of $a = b = 5.66$ Å and $c = 11.28$ Å (Figure 1b). XRD results of pristine Cu_3SbSe_4 NCs and NCs containing different amounts of Pb demonstrate well-defined diffraction peaks with no impurity phases. Focusing on the most intense diffraction peak located *ca.* 27.5°, associated with the (112) lattice plane, it is evident that the XRD pattern of $Cu_3Sb_{1-x}Pb_xSe_4$ (x=0.01, 0.02, and 0.03) shifts to low angles with the introduction of Pb (Figure 1d). This phenomenon indicates a lattice distortion caused by the large Pb replacing smaller atoms within the lattice, as confirmed by estimates derived using the Williamson-Hall formalism (Figure S1, Table S1, the details can be found in the supporting information). On the other hand, the size and shape distribution of the as-prepared NCs remains unchanged after Pb-doping (Figure S2). Quantitatively, within the experimental error, the Pb content matches the nominal composition of $Cu_3Sb_{1-x}Pb_xSe_4$ (x = 0, 0.01, 0.02, and 0.03), with only a slight excess of Se, as evidenced by X-ray spectroscopy (EDX) (Figure S3) and inductively coupled plasma optical emission spectroscopy (ICP-OES) (Table S2). The decrease in the amount of Sb following the nominal precursor concentration indicates that Pb most probably occupies the Sb sites left by the lack of enough Sb.

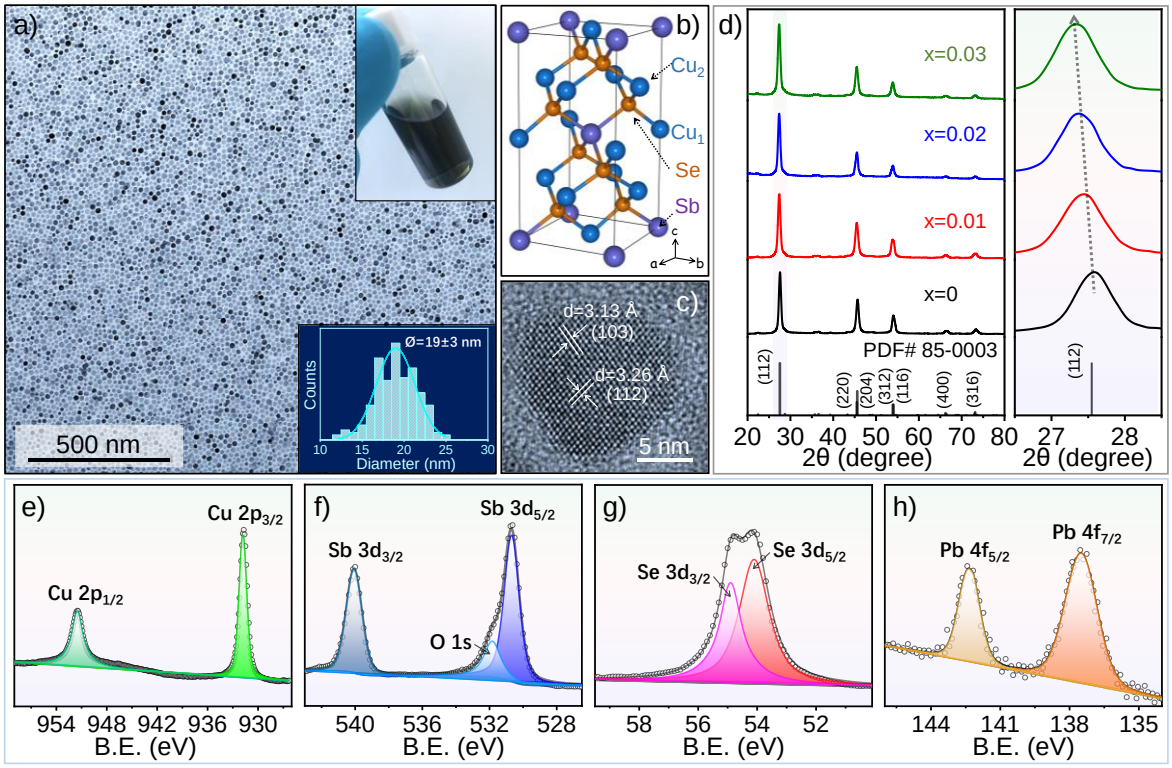

Figure 1. (a) TEM micrograph of the Cu_3SbSe_4 NCs. The upper inset shows NCs dispersed in chloroform and the bottom inset shows the histogram for the measured particle size distribution. (b) The unit cell of tetragonal Cu_3SbSe_4. (c) HRTEM image of a single Cu_3SbSe_4 NC. (d) XRD patterns of pristine Cu_3SbSe_4 and $Cu_3Sb_{1-x}Pb_xSe_4$ (x = 0.01, 0.02, and 0.03) NCs including the PDF 85–0003 reference of Cu_3SbSe_4 (black vertical lines), with the pattern on the right showing a detail of the (112) peak. (e-h) High-resolution XPS spectrum of $Cu_3Sb_{0.97}Pb_{0.03}Se_4$ NCs: (e) Cu 2p, (f) Sb 3d, (g) Se 3d, and (h) Pb 4f.

X-ray Photoelectron Spectroscopy (XPS) was employed to investigate the chemical state of the elements in the synthesized Pb-doped Cu_3SbSe_4 NCs (Figure 1e-h). In the as-synthesized $Cu_3Sb_{0.97}Pb_{0.03}Se_4$ NCs, the two peaks in the Cu 2p spectrum appear at 931.7 eV ($2p_{3/2}$) and 951.6 eV ($2p_{1/2}$), consistent with the standard separation of 19.9 eV and indicative of Cu (I) (Figure 1e).[41,46] The presence of Cu^{2+} was excluded by the absence of the satellite peaks characteristic of this higher oxidation state of Cu.[47] Moreover, Cu-LMM Auger energy peak, observed at 570 eV as shown in Figure S4b, further indicates no signs of metallic Cu^0 (568 eV) or oxidized Cu^{2+} (568.9 eV), in accordance with previous studies.[48–50] Figure 1f shows the Sb 3d XPS spectrum that displays a doublet associated with Sb^{5+} at 530.6 and 540.1 eV for Sb $3d_{5/2}$

and Sb $3d_{3/2}$, respectively.[41,51] Additionally, the overlapping O 1s peak centered at 531.9 eV is related to the presence of some surface oxygenated groups.[12,52] The Se 3d XPS spectrum (Figure 1g) shows a doublet at 54.2 eV for $3d_{5/2}$ and 55.1 eV for $3d_{3/2}$ which is associated with a Se^{2-} oxidation state.[21,46,53] Additionally, the Se 3p electronic levels are detected at 161.1 eV ($3p_{3/2}$) and 166.8 eV ($3p_{1/2}$), demonstrating a peak splitting of 5.7 eV, corresponding well with previous reports (Figure S4c).[21,41,46,54] Figure 1h shows the high-resolution spectrum of the Pb 4f region, revealing the two main characteristic peaks of Pb 4f at 137.6 and 142.4 eV, corresponding to Pb $4f_{7/2}$ and Pb $4f_{5/2}$, respectively, originating from the Pb^{2+} in $Cu_3Sb_{0.97}Pb_{0.03}Se_4$ NCs.[55–57] Thus, XPS results validate that Pb^{2+} stands as the stable and prevalent valence state for Pb, which is not consistent with previous reports considering Pb in a Pb^{4+}chemical state.[45]

Two sequential processes of ligand displacement and annealing were used to mitigate the influence of organic ligands on the electrical transport performance of the subsequent densified bulk pellet and to secure their thermal stability (experimental details can be found in the "Experimental" section). Specifically, the morphology of the $Cu_3Sb_{0.97}Pb_{0.03}Se_4$ powder treated through the above step process can be found in Figure S4.

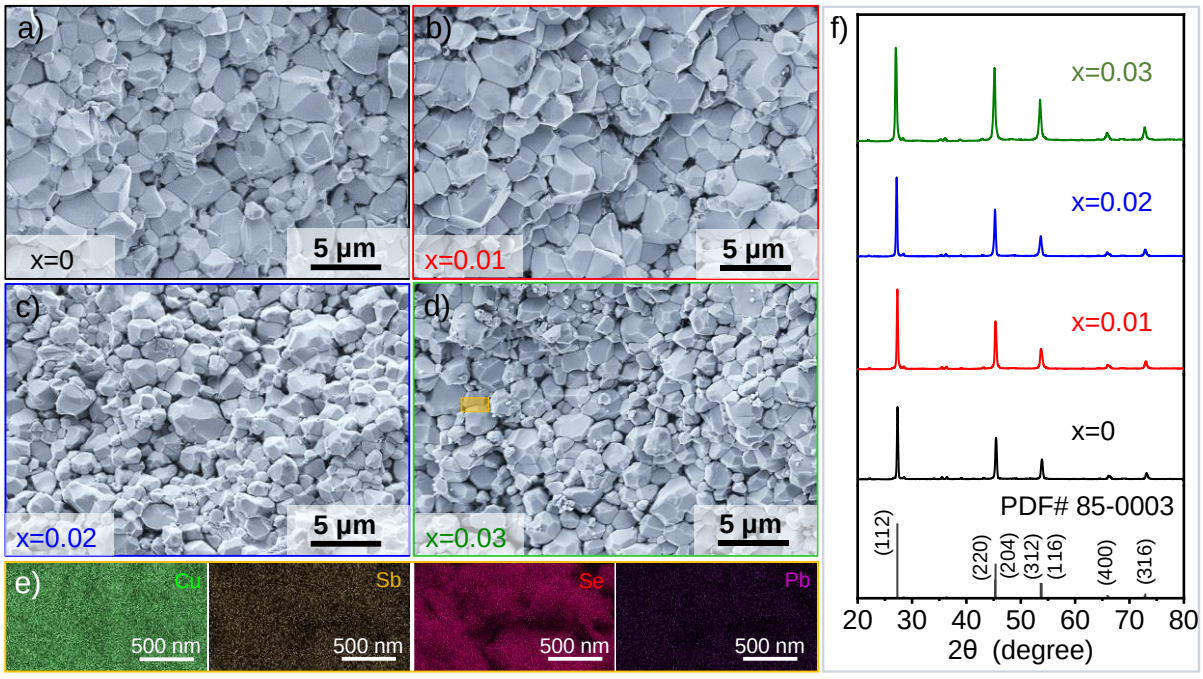

Figure 2. (a)-(d) Representative SEM images of the fractured surfaces of pellets obtained from $Cu_3Sb_{1-x}Pb_xSe_4$ (x=0, 0.01, 0.02, and 0.03) NCs, respectively; (e) EDX elemental maps of $Cu_3Sb_{0.97}Pb_{0.03}Se_4$ pellet in the orange region of Figure 2d, including Cu, Sb, Se and Pb, respectively; (f) Corresponding XRD patterns of $Cu_3Sb_{1-x}Pb_xSe_4$ (x=0, 0.01, 0.02, and 0.03) pellets, including the Cu_3SbSe_4 reference pattern (PDF 85–0003).

To evaluate their TE performance, the treated $Cu_3Sb_{1-x}Pb_xSe_4$ (x=0.01, 0.02, and 0.03) nanopowders were hot-pressed at 380°C and 70 MPa for 10 min. This process consolidated the powder into bulk pellets (Ø10 mm × h=1.5 mm). The relative densities of all obtained pellets were above 93% of the theoretical value (Table S3) and showed robust mechanical properties. SEM characterization of fractured pellets (**Figure 2**a-d) reveals that during the consolidation process, the annealed particles underwent additional growth, which led to the formation of larger grains, ranging in size from hundreds of nanometers to several micrometers. Such significant grain growth at these temperatures can be rationalized by the annealing mechanism and the thermodynamic properties of the materials. The proximity to the material's peritectic temperature, as delineated by the phase diagram,[58] the combined effects of the elevated surface energy of the particles and the supplementary energy introduced through hot pressing provides a considerable driving force to enhance atomic mobility. This enhanced atomic mobility promotes the coalescence of particles into larger grains.[21,59,60] On the other hand, the samples with higher Pb content (>2%) exhibit abundant nanoscale grains (Figures 2c and 2d). In addition, the EDX compositional maps revealed a relatively homogeneous distribution of Pb at a 500 nm scale, as shown in Figure 2e, corresponding to the orange region in Figure 2d. XRD patterns of $Cu_3Sb_{1-x}Pb_xSe_4$ (x=0.01, 0.02, and 0.03) pellets revealed no structural changes and the emergence of no secondary phases upon the thermal treatment and consolidation processes (Figure 2f). A shift of the XRD peaks to lower angles exhibited an expansion of the lattice parameters and volume of unit cell with increasing Pb content in the $Cu_3Sb_{1-x}Pb_xSe_4$ (x=0.01,

0.02, and 0.03) pellets (Figure S6), which is consistent with the XRD patterns of NCs (Figure 1d), indicating the substitution of Sb^{5+} by Pb^{2+} ions.

Figure 3 illustrates the electrical transport properties of $Cu_3Sb_{1-x}Pb_xSe_4$ (x = 0, 0.01, 0.02, and 0.03) pellets as a function of temperature over the temperature range of *ca.* 310 to 650 K. The pristine Cu_3SbSe_4 exhibits low σ, *ca.* 21.6 S cm^{-1} at room temperature, which increases to 50.1 S cm^{-1} at 650 K. The increase of σ with temperature denotes the thermal excitation of charge carriers to play an increasingly important role, which agrees with previous reports (Figure 3a).[34,41] The σ of all $Cu_3Sb_{1-x}Pb_xSe_4$ (x = 0, 0.01, 0.02, 0.03) samples consistently display significantly higher σ values in comparison to undoped Cu_3SbSe_4, *e.g.*, the $Cu_3Sb_{0.97}Pb_{0.03}Se_4$ sample reaches an exceptional σ of 98.1 S cm^{-1} at room temperature, approximately 5 times larger than the value of the undoped Cu_3SbSe_4. While the doped sample with a lower Pb amount shows a similar temperature dependence of σ as Cu_3SbSe_4, the $Cu_3Sb_{0.98}Pb_{0.02}Se_4$ and especially the $Cu_3Sb_{0.97}Pb_{0.03}Se_4$ samples exhibit a decrease of σ with temperature in the low-temperature range tested, denoting a degenerated semiconductor behavior.

High *S* values were obtained in Cu_3SbSe_4, which can be ascribed to the intricate electronic structure inherent to Cu_3SbSe_4, characterized by the presence of multiple energy bands. This complexity engenders the existence of numerous electronic transport pathways, spanning across various energy bands, which significantly contributes to the rise of *S*.[34,41] All $Cu_3Sb_{1-x}Pb_xSe_4$ pellets possess an intrinsic *p*-type semiconductor nature, as positive *S* values were consistently obtained across the entire temperature range (Figure 3b). The *S* values of all pellets exhibit an initial increase followed by a subsequent descent with rising temperature, *e.g.* the pristine Cu_3SbSe_4 displays a *S* value of *ca.* 399 μV/K at room temperature that progressively diminishes to *ca.* 339 μV/K at 650 K, in accordance with our previous report.[41] Upon the introduction of substantial Pb doping, as exemplified by the $Cu_3Sb_{0.97}Pb_{0.03}Se_4$ pellet, this behavior undergoes significant attenuation and shifts towards a degenerate semiconductor mode, consistent with

the significant increase in σ, owing to the gradual thermal excitation of charge carriers.

Room temperature Hall measurements were conducted to determine the Hall charge carrier concentration, p_H, and mobility, μ_H. Figure 3c shows that the p_H of undoped Cu_3SbSe_4 is only 0.45×10^{19} cm^{-3}. With the addition of 3% Pb, there is a noticeable increase in p_H~3×10^{19} cm^{-3} for $Cu_3Sb_{0.97}Pb_{0.03}Se_4$, which is more than 6 times higher than that of undoped Cu_3SbSe_4. The μ_H at room temperature is relatively lower in all Pb-doped samples compared to undoped Cu_3SbSe_4 (Figure 3c). This result is associated with the larger density of charge scattering centers and potentially with the existence of heavy holes related to an increase in the density of states (DOS) effective mass (m_d*). To clarify this last point, the m_d* values were estimated using the single parabolic band (SPB) model, which includes all contributions from various valence bands (Figure S7a). The Pisarenko plot at 300 K showing S as the vertical coordinate and p_H as the horizontal coordinate confirms a significant increase in the m_d* value for Cu_3SbSe_4 upon Pb introduction (Figure 3e), as indicated by the increase in the discrepancy between the measured data points and the calculated values. This result is consistent with the electronic structure calculations below (**Figure 4**). This increase in m_d* values explain the superior S values achieved by all Pb-doped samples at room temperature.

We further calculated the weighted mobilities (μ_W) of $Cu_3Sb_{1-x}Pb_xSe_4$ (x = 0, 0.01, 0.02, and 0.03) using the S and σ values to examine the underlying transport phenomenon based on the equation:

$$\mu_W = \frac{3h^3\sigma}{8\pi e(2m_e k_B T)^{3/2}}\left[\frac{exp\left[\frac{e|S|}{k_B}-2\right]}{1+exp\left[\frac{-5e|S|}{k_B}+5\right]}+\frac{\frac{3}{\pi^2}\frac{e|S|}{k_B}}{1+exp\left[\frac{5e|S|}{k_B}-5\right]}\right] \quad (1)$$

In the above equation h, κ_B, e, and m_e, are Plank's constant, Boltzmann's constant, electron charge, and electron mass, respectively.[61] The results are shown in Figure 3f. μ_W increases with raising p_H, different from the decrease in μ_H observed in $Cu_3Sb_{1-x}Pb_xSe_4$ samples, resulting in a significant increase in the deviations between μ_W and μ_H for all samples, *i.e.*, the μ_W/μ_H values

more conspicuously underscore the amplification of this disparity, providing a quantitative elucidation of the enlarged m_d* associated with the increment in p_H,[62] *e.g.*, in comparison to Cu_3SbSe_4 with p_H~0.45×10^{19} cm^{-3}, $Cu_3Sb_{0.97}Pb_{0.03}Se_4$, featuring p_H~3×10^{19} cm^{-3}, achieves an increase in the μ_W/μ_H value of over 2-fold (inset in Figure 3f). This increase also indicates a larger m_d*, which is consistent with the estimation provided by the SPB model.

The σ and S values of $Cu_3Sb_{1-x}Pb_xSe_4$ (x = 0, 0.01, 0.02, and 0.03) were used to calculate the power factors ($PF = \sigma S^2$) shown in Figure 3d. The PFs of the Pb-doped materials are significantly greater than those of undoped Cu_3SbSe_4. Among these samples, $Cu_3Sb_{0.97}Pb_{0.03}Se_4$ exhibits the maximum PF values in the entire range of temperatures, reaching *ca.* 0.92 mW m^{-1}K^{-2} at 655 K, much larger than pristine Cu_3SbSe_4 and higher than the previously reported values for Cu_3SbSe_4-based compounds.[41,42,45,63]

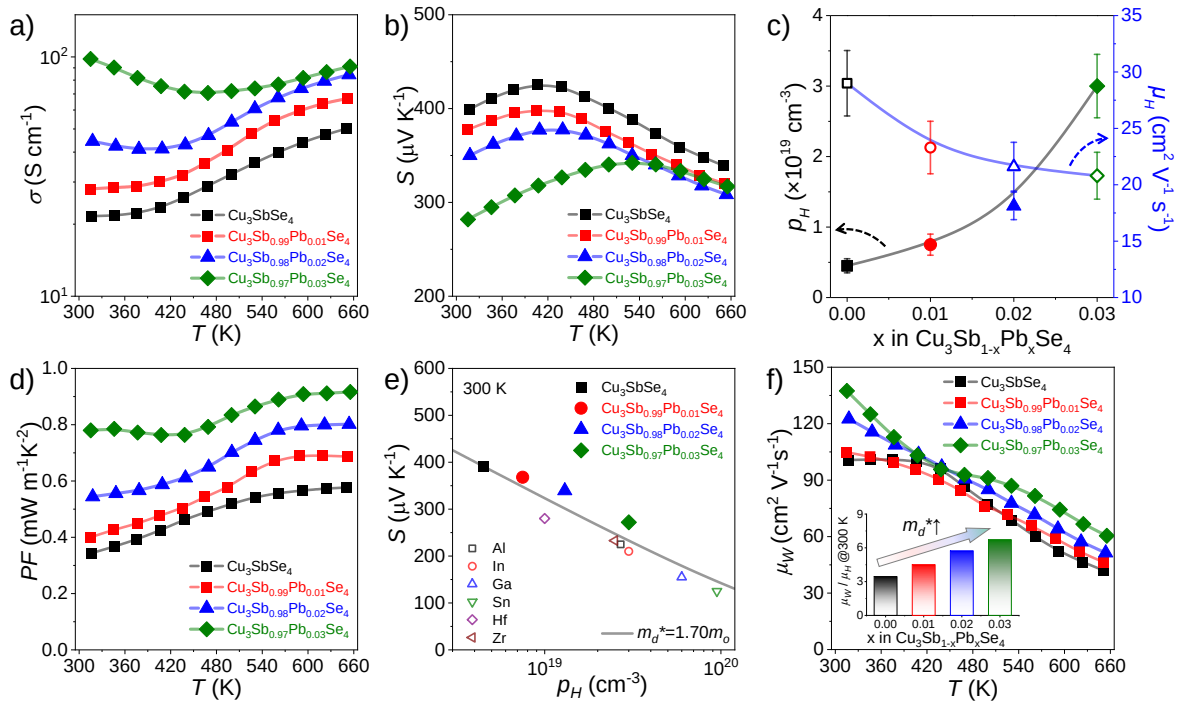

Figure 3. Electrical transport properties of $Cu_3Sb_{1-x}Pb_xSe_4$ (x=0, 0.01, 0.02, and 0.03). (a,b) Temperature dependence of (a) electric conductivity (σ) and (b) Seebeck coefficient (S); (c) Ambient temperature Hall charge carrier concentration (p_H) and carrier mobility (μ_H); (d) Temperature dependence of power factors (PF); (e) Pisarenko plot at 300 K, and the open dots represent reported Cu_3SbSe_4-based systems;[34,39,63] (f) Weighted mobility (μ_W) as a function of temperature, the inset shows μ_W /μ_H as a function of x in $Cu_3Sb_{1-x}Pb_xSe_4$ (x=0, 0.01, 0.02, and

0.03) at room temperature indicates an increasing trend of m_d*.

To investigate the influence of Pb doping on the band structure of Cu_3SbSe_4, we conducted DFT calculations (Figure 4). Figures 4a and 4b display the calculated band structure and DOS for Cu_3SbSe_4. The computed band gap (E_g) is *ca.* 0.16 eV, which is lower than the reported value of 0.29 eV for Cu_3SbSe_4,[34,37] in agreement with previous experimental values (0.1−0.4 eV).[38,64,65] Despite the bandgap underestimation due to the inherent complexities in calculations, DFT offers valuable insight into the evolution of the band structure post-Pb doping. The band structure of Cu_3SbSe_4 displays two valence band edges, one positioned at Γ and the other between points Z and R, with a slight energy offset. Figures 4c and 4d depict the calculated band structure and DOS for Pb-doped Cu_3SbSe_4. Pb doping shifts the Fermi level from the bandgap region into the valence band, indicating an increase in p_H, agreeing with the experimental measurement in Figure 3c. The DFT calculations reveal a slight decrease in the *Eg* with Pb doping, which is consistent with previous first-principles studies, indicating that substitution of Sb with elements from both Group IIIA (*e.g.*, Al, Ga, In, Tl) and Group IVA (*e.g.,* Ge, Sn, Pb) leads to a reduction in the *Eg*.[37] In addition, the bipolar conduction is suppressed due to the increased p_H through Pb doping, as evidenced by the shift of the *S* peak to higher temperatures (Figure 3b). Moreover, Pb doping decreases the energy offset between the two valence band edges at the Γ point and between Z and R points implying more pathways for carrier transport, which further explains the observed high *PFs* in $Cu_3Sb_{1-x}Pb_xSe_4$. From the calculated band structures, we can attribute the enhanced *PF*s to the increased p_H and the valence band convergence effects induced by Pb doping.

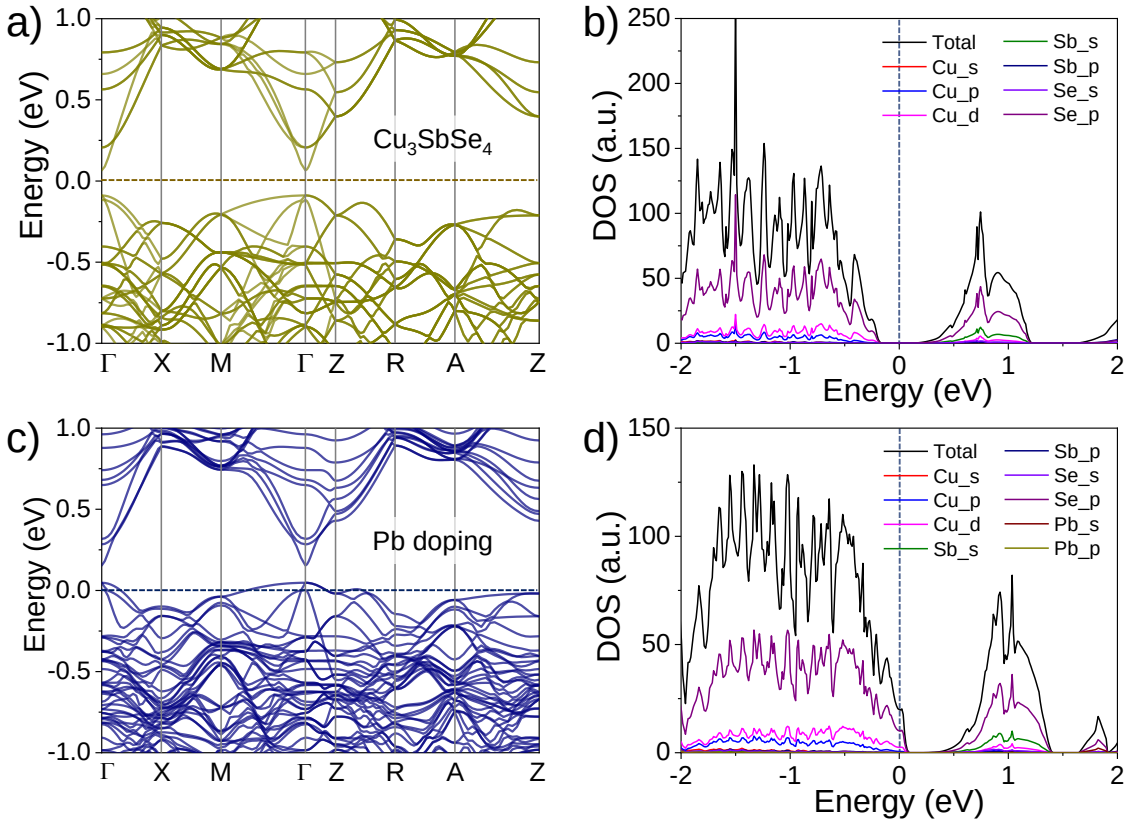

Figure 4. (a) Calculated band structure and (b) DOS of Cu_3SbSe_4. (c) Calculated band structure and (d) DOS of Pb-doped Cu_3SbSe_4.

The κ_{tot} of all $Cu_3Sb_{1-x}Pb_xSe_4$ (x = 0, 0.01, 0.02, and 0.03) pellets consistently decreases with temperature throughout the whole temperature range measured, yielding relatively low values as shown in **Figure 5**a (the experimental heat capacity C_p and thermal diffusivity λ can be found in Figures S7c and S7d). Specifically, in the pristine Cu_3SbSe_4, the κ_{tot} value drops to 0.70 W m^{-1} K^{-1} at 650 K, which is lower than the values reported for most bulk Cu_3SbSe_4 materials.[34,39,40,43,66,67] We calculated κ_L (Figure 5b) and κ_e (Figure 5c) of all the samples by the Wiedemann–Franz law: $\kappa_e = L_o\sigma T$ and $\kappa_L = \kappa_{tot} - \kappa_e$, where L_o is the Lorenz number calculated based on the measured S values (Figure S7b).[68] Figure 5b shows the very low κ_L values obtained for all samples and particularly for $Cu_3Sb_{0.97}Pb_{0.03}Se_4$ that reaches an ultralow $\kappa_L \approx$ 0.61 W m^{-1} K^{-1} at 655 K, which is significantly lower than those previously reported for samples prepared by solid-state methods,[34,39,40,43,66,69] but is still above the theoretical limit for the amorphous state (κ_{Lmin}~0.47 W $m^{-1}K^{-1}$).[34] This low κ_L value obtained for $Cu_3Sb_{0.97}Pb_{0.03}Se_4$

in the high-temperature domain is mainly attributed to the introduction of lattice distortions due to the presence of much larger radius Pb^{2+} in the doped material obtained in the present work, as well as to the high-density interfaces, *i.e.*, presence of more and smaller grains. The observed increase in κ_L at lower temperatures in samples with higher Pb content, exhibiting a similar trend to previous reports,[45,70] could be attributed to the complex interplay between the dopant concentration and the crystal lattice, demanding further investigation. The inset in Figure 5b illustrates the plot of κ_L for $Cu_3Sb_{1-x}Pb_xSe_4$ as a function of the reciprocal of 1000/T, from which all κ_L exhibit a nearly linear relationship, indicating the crucial role of Umklapp phonon scattering in Cu_3SbSe_4.[71]

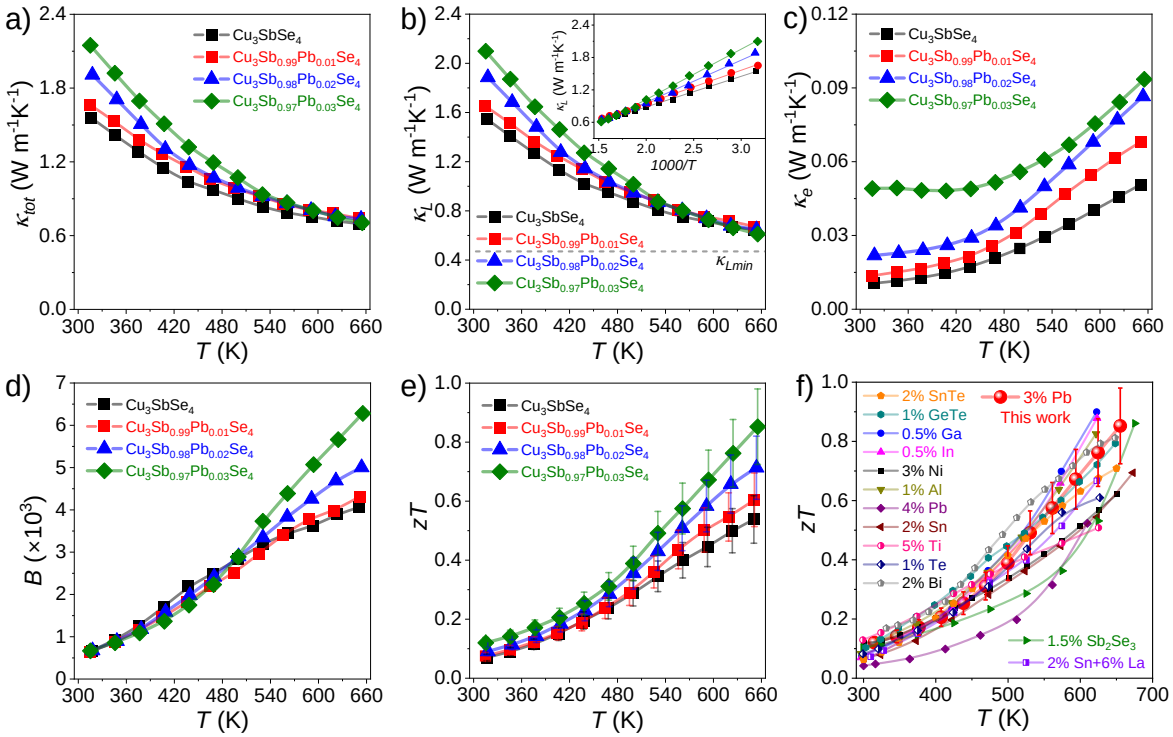

Figure 5. Temperature dependence of (a) total thermal conductivity, κ_{tot}; (b) lattice thermal conductivity, κ_L, and the inset shows the plot of 1000/T-dependent κ_L; (c) electronic thermal conductivity, κ_e; (d) quality factor, B; (e) TE figure of merit, zT, and (e) zT values for reported state-of-the-art *p*-type doped Cu_3SbSe_4-based materials and composites, including 2%SnTe,[72] 1%GeTe,[67] 1.5%Bi_2Se_3,[69] 2%Sn+6%La,[43] 0.5%Ga,[39] 0.5%In,[39] 3%Ni,[40] 1%Al,[39] 4%Pb,[45] 2%Sn,[34] 5%Ti,[42] 1%Te[73] and 2%Bi[41].

The quality factor B was calculated using the following equation:[56,62]

$$B = 9\frac{\mu_W}{\kappa_L}\left(\frac{T}{300}\right)^{5/2} \quad (2)$$

B is directly proportional to μ_W/κ_L, making it a valuable parameter for evaluating the overall TE performance of a particular material. As shown in Figure 5d, B increases almost linearly with temperature for all samples over the entire temperature range and increases with Pb content, especially in the high-temperature region beyond 500 K.

Overall, the synergistic improvement in electrical and thermal transport properties allows achieving a zT_{max} value of 0.85 at 655 K for $Cu_3Sb_{0.97}Pb_{0.03}Se_4$ (Figures 5e and S7f), which is 1.6 times that of undoped Cu_3SbSe_4 in the present work and is higher than most of the excellent performing doped Cu_3SbSe_4-based materials and composites prepared via solid-state and/or solution-processed methods (Figure 5f).[34,39–43,45,67,69,72,73] Furthermore, the results obtained for $Cu_3Sb_{0.97}Pb_{0.03}Se_4$ pellets exhibit excellent reproducibility between different samples, as shown in Figure S8. Compared to conventional solid-state synthesis methods commonly used for Cu_3SbSe_4-based TE materials, this solution-processed approach for Pb-doped Cu_3SbSe_4 NCs offers cost-effectiveness and environmental friendliness while operating at lower temperatures and ambient pressures, utilizing lower-purity precursors, and reducing production costs. In addition, this method enables the fabrication of Pb-doped Cu_3SbSe_4-based nanocomposites, allowing for versatile material design and optimization for specific TE applications.

3. Conclusion

In this study, we reported a colloidal synthesis route to produce Cu_3SbSe_4 NCs in high yield and scalability. We thoroughly investigated the electrical transport properties of these compounds doped with different amounts of Pb, and found that Pb doping significantly increased the σ with a relatively high S due to the increase in p_H and larger enhanced m_d*, which greatly improved PF. In addition, the introduction of large ionic radii of Pb^{2+} also led to lattice distortions while also contributing to an increase in the density of nanostructured point defects,

which drastically reduced the κ_L at high temperatures. Based on the above synergistic modulation of thermal and electrical transport properties, the zT_{max} of 0.85 at 655 K was obtained for $Cu_3Sb_{1-x}Pb_xSe_4$. These findings underscore the promising potential of Pb-doped Cu_3SbSe_4 compounds for medium-temperature TE applications, representing a significant stride towards the development of efficient TE materials and devices.

4. Experimental section

Chemicals and solvents: Copper(I) chloride (CuCl, ≥99%), antimony(III) chloride ($SbCl_3$, 99%), selenium powder (Se, 99.5%), ammonium thiocyanate (NH_4SCN, ≥99%), lead(II) acetate trihydrate ($Pb(OAc)_2 \cdot 3H_2O$, 99.5%), dodecanethiol (DDT, 98%), 1-octadecene (ODE, technical grade 90%), oleic acid (OA, technical grade 99%), and oleylamine (OLA, technical grade 70%) were purchased from Aladdin, China. Analytical grade ethanol and chloroform were obtained from Sinopharm Chemical Reagent Co., Ltd. All chemicals were used as received without further purification.

Large-scale synthesis of Cu_3SbSe_4 NCs and $Cu_3Sb_{1-x}Pb_xSe_4$ NCs: The synthesis method followed the original recipe with minor modifications.[41] A 0.5 M selenium stock solution was prepared initially by adding Se powder (60 mmol) into a 250 mL three-neck flask containing OLA (60 mL) and DDT (60 mL) at room temperature under magnetic stirring. To eliminate air from the flask, three cycles of vacuum and nitrogen purging were conducted until the Se powder dissolved entirely. Simultaneously, a combination of CuCl (12.0 mmol), $SbCl_3$ (4.8 mmol), OLA (18 mL), OA (12 mL), and ODE (120 mL) was prepared in a 500 mL three-neck flask. The mixture was stirred at room temperature for 20 min. Then, the solution was heated to 130 °C under vacuum with vigorous stirring and held there for 30 min. After that, nitrogen gas was introduced, and the temperature was increased to 180°C. At this point, a quick injection of the pre-prepared 60 mL Se precursor solution caused an instant color change, from brown to deep green, in the reaction solution. The color change signifies the nucleation of Cu_3SbSe_4 NCs. The

reaction solution was maintained at 180 °C for 30 min. Afterward, the colloidal solution was cooled rapidly to room temperature using a water bath. Chloroform was utilized as the dispersion solvent, while ethanol served as the antisolvent. The crude solution was centrifuged at 8000 rpm for 5 min, and the resulting supernatant was decanted. This process was repeated twice, after which the obtained powder was re-suspended in chloroform and stored for eventual characterization and utilization.

The preparation process of $Cu_3Sb_{1-x}Pb_xSe_4$ (x = 0.01, 0.02, and 0.03) NCs was identical to that of the original Cu_3SbSe_4 NCs, except that appropriate amounts of $Pb(OAc)_2{\cdot}3H_2O$ replaced some of the $SbCl_3$. The reactants were used at molar ratios of $SbCl_3/Pb(OAc)_2{\cdot}3H_2O$=0.99/0.01 (4.752 mmol/0.048 mmol), 0.98/0.02 (4.704 mmol/0.096 mmol), and 0.97/0.03 (4.656 mmol/0.144 mmol).

Ligand displacement and annealing treatments: In a typical procedure, $Cu_3Sb_{1-x}Pb_xSe_4$ (x = 0, 0.01, 0.02, and 0.03) NCs (~2 g) were first dispersed in 50 mL of chloroform and mixed with 10 mL of a 50 mM NH_4SCN solution (in acetone) at room temperature. The solution was shaken for 1 min to displace the organic ligands attached to the NCs surface, followed by precipitation of the NCs by centrifugation. This process was repeated one more time, adding chloroform and NH_4SCN in each step. Finally, NCs were precipitated and dried under vacuum to obtain a fine powder. The dried $Cu_3Sb_{1-x}Pb_xSe_4$ (x = 0, 0.01, 0.02, and 0.03) nanopowders underwent annealing in a tube furnace under N_2 flow, heated at a rate of 10 °C/min to 400 °C, and maintained for 1 hour. After this process, the annealed powders were promptly transferred to a glovebox for the subsequent densification.

Nanopowder consolidation into pellets: The annealed $Cu_3Sb_{1-x}Pb_xSe_4$ (x = 0, 0.01, 0.02, and 0.03) nanopowders were ground inside the glovebox with an agate mortar followed by loading into a graphite die lined with 0.20 mm thick graphite paper. These powders were then compacted into pellets (Ø10 mm × h = 1.5 mm) in a nitrogen atmosphere using a custom-made hot press by applying an uniaxial pressure of 70 MPa at 380 °C for 10 min. The density of all

the pressed pellets was above 93% (Table S3) of the theoretical value (5.86 g/cm^3). Finally, all the pellets were annealed in a nitrogen gas static atmosphere for 1 h at 350 °C (*ca.* 4 °C/min).

Structural and chemical characterization: XRD analyses were performed on a Bruker AXS D8 Advance X-ray diffractometer with Cu Kα radiation (Germany, λ= 0.15406 Å), scanning from 20° to 80° with a resolution of 0.01° and a time step of 0.1 s. The size and shape of the initial NCs were examined by TEM using a Zeiss Libra 120, operating at 120 kV, and HRTEM images were recorded using a JEOL JEM-2200FS microscope operating at 200 kV. Field-emission SEM was conducted at 5.0 kV using an Auriga Zeiss SEM to detect the grain size and morphology of the pressed materials. Quantitative elemental analysis of $Cu_3Sb_{1-x}Pb_xSe_4$ NCs' overall composition was carried out through energy-dispersive EDX detection connected to the SEM instrument, operating at 15.0 kV and by ICP-OES on the ICPE-9820 system. XPS was performed in constant analyzer energy mode on a VG ESCA Scientific Theta Probe Spectrometer with a pass energy of 28 eV and aluminum Ka (1486.6 eV) radiation as the excitation source.

Thermoelectric property measurement: Both σ and S were simultaneously measured utilizing a Linseis system (LSR-3) with a heating rate of 10 K/min under a helium atmosphere in the temperature range from 310 to 650 K. An estimated error of approximately 4% was accounted for in the measurements. Thermal diffusivity (λ) was measured using the Linseis LFA 1000 Laser Flash analysis instrument with an estimated error of about 5%. The κ_{tot} was calculated using the formula $\kappa_{tot} = \lambda C_p \rho$, where C_p represents specific heat capacity, and ρ refers to mass density. The values for C_p, dependent on temperature, were measured through the differential scanning calorimetry (DSC 404 F3, Netzsch) method and calculated via Netzsch Proteus software, employing the C_p ratio method with a sapphire standard. For comparison, the constant pressure C_p was also determined using empirical formulas based on the Dulong–Petit limit (3R law). The Dulong–Petit C_p value was slightly lower than the experimental C_p values (Figure S7d). We present a comparison of κ_{tot} and zT values obtained when considering either

the experimentally determined C_p or the calculated C_p in Figures S7e and S7f. The ρ values (Table S3) were determined using the Archimedes method with an error of *ca.* 2%. Therefore, the plot presents a combined estimation of approximately 17% uncertainty for all measurements of electrical and thermal transport properties involved in determining *zT*. Furthermore, p_H and μ_H measurements were conducted at 300 K using a Hall measurement system (PPMS-9T, Quantum Design Inc., USA) under a magnetic field of 2 T, with an error of approximately 10%.

DFT calculations: DFT calculations were conducted using the Vienna ab initio simulation package (VASP)[74–76] with post-processing VASPKIT package.[77] It was reported that it was necessary to use the generalized gradient approximations (GGA) with a large Hubbard U value to estimate bandgap values.[38,64] We used an U of 15 eV. To consider the impact of Pb doping, a 2 × 2 × 2 supercell structure of $Cu_{48}Se_{64}Sb_{16}$ based on the tetragonal cell was built. By randomly replacing one Sb, the composition of $Cu_{48}Se_{64}Sb_{15}Pb$ was obtained. The structures were relaxed until the total energy < 10^{-5} eV and the force on atoms < 0.01 eV $Å^{-1}$.

Supporting Information

Supporting Information is available from the Wiley Online Library or from the author.

Acknowledgements

Y.L. acknowledges funding from the National Natural Science Foundation of China (NSFC) (Grants No. 22209034), the Innovation and Entrepreneurship Project of Overseas Returnees in Anhui Province (Grant No. 2022LCX002). K.H.L. acknowledges financial support from the National Natural Science Foundation of China (Grant No. 22208293). M.I. acknowledges financial support from ISTA and the Werner Siemens Foundation.

Author Contributions

The manuscript was written through the contributions of all authors. All authors have approved the final version of the manuscript.

Conflict of Interest

The authors declare no conflict of interest.

Received: ((will be filled in by the editorial staff))
Revised: ((will be filled in by the editorial staff))
Published online: ((will be filled in by the editorial staff))

References

[1] X. L. Shi, J. Zou, Z. G. Chen, *Chem. Rev.* **2020**, *120*, 7399.

[2] G. Tan, L.-D. Zhao, M. G. Kanatzidis, *Chem. Rev.* **2016**, *116*, 12123.

[3] L. E. Bell, *Science* **2008**, *321*, 1457.

[4] M. Zebarjadi, K. Esfarjani, M. S. Dresselhaus, Z. F. Ren, G. Chen, *Energy Environ. Sci.* **2012**, *5*, 5147.

[5] S. Ortega, M. Ibáñez, Y. Liu, Y. Zhang, M. V. Kovalenko, D. Cadavid, A. Cabot, *Chem. Soc. Rev.* **2017**, *46*, 3510.

[6] M. Ibáñez, Z. Luo, A. Genç, L. Piveteau, S. Ortega, D. Cadavid, O. Dobrozhan, Y. Liu, M. Nachtegaal, M. Zebarjadi, J. Arbiol, M. V Kovalenko, A. Cabot, *Nat. Commun.* **2016**, *7*, 10766.

[7] J. He, T. M. Tritt, *Science* **2017**, *357*, aak9997.

[8] Y. Liu, M. Ibáñez, *Science* **2021**, *371*, 678.

[9] X. Tang, Z. Li, W. Liu, Q. Zhang, C. Uher, *Interdiscip. Mater.* **2022**, *1*, 88.

[10] M. Hong, M. Li, Y. Wang, X.-L. Shi, Z.-G. Chen, *Adv. Mater.* **2023**, *35*, 2208272.

[11] Y. Zhang, C. Xing, Y. Liu, M. C. Spadaro, X. Wang, M. Li, K. Xiao, T. Zhang, P. Guardia, K. H. Lim, A. O. Moghaddam, J. Llorca, J. Arbiol, M. Ibáñez, A. Cabot, *Nano Energy* **2021**, *85*, 105991.

[12] Y. Liu, M. Li, S. Wan, K. H. Lim, Y. Zhang, M. Li, J. Li, M. Ibáñez, M. Hong, A. Cabot, *ACS Nano* **2023**, *17*, 11923.

[13] M. Calcabrini, A. Genc, Y. Liu, T. Kleinhanns, S. Lee, D. N. Dirin, Q. A. Akkerman, M. V. Kovalenko, J. Arbiol, M. Ibañez, *ACS Energy Lett.* **2021**, *6*, 581.

[14] K. H. Lim, M. Li, Y. Zhang, Y. Wu, Q. Zhou, Q. Wang, X. Yang, P. Liu, W.-J. Wang, K. W. Wong, K. M. Ng, Y. Liu, A. Cabot, *J. Mater. Sci. Technol.* **2024**, *171*, 71.

[15] S. Roychowdhury, T. Ghosh, R. Arora, M. Samanta, L. Xie, N. K. Singh, A. Soni, J. He, U. V. Waghmare, K. Biswas, *Science* **2021**, *371*, 722.

[16] Y. Xiao, L. D. Zhao, *Science* **2020**, *367*, 1196.

[17] C. Chang, B. Qin, L. Su, L.-D. Zhao, *Sci. Bull.* **2022**, *67*, 1105.

[18] M. Ibáñez, R. Hasler, A. Genç, Y. Liu, B. Kuster, M. Schuster, O. Dobrozhan, D. Cadavid, J. Arbiol, A. Cabot, V. M. Kovalenko, *J. Am. Chem. Soc.* **2019**, *141*, 8025.

[19] J. P. Heremans, V. Jovovic, E. S. Toberer, A. Saramat, K. Kurosaki, A. Charoenphakdee, S. Yamanaka, G. J. Snyder, *Science* **2008**, *321*, 554.

[20] Y. Liu, M. Calcabrini, Y. Yu, S. Lee, C. Chang, J. David, T. Ghosh, M. C. Spadaro, C. Xie, O. Cojocaru-Mirédin, J. Arbiol, M. Ibáñez, *ACS Nano* **2022**, *16*, 78.

[21] Y. Liu, M. Calcabrini, Y. Yu, A. Genç, C. Chang, T. Costanzo, T. Kleinhanns, S. Lee, J. Llorca, O. Cojocaru-Mirédin, M. Ibáñez, *Adv. Mater.* **2021**, *33*, 2106858.

[22] M. Hong, Z.-G. Chen, *Acc. Chem. Res.* **2022**, *55*, 3178.

[23] K. Biswas, J. He, I. D. Blum, C. I. Wu, T. P. Hogan, D. N. Seidman, V. P. Dravid, M. G. Kanatzidis, *Nature* **2012**, *489*, 414.

[24] B. Jiang, Y. Yu, J. Cui, X. Liu, L. Xie, J. Liao, Q. Zhang, Y. Huang, S. Ning, B. Jia, B. Zhu, S. Bai, L. Chen, S. J. Pennycook, J. He, *Science* **2021**, *371*, 830.

[25] C. Xing, Y. Zhang, K. Xiao, X. Han, Y. Liu, B. Nan, M. G. Ramon, K. H. Lim, J. Li, J. Arbiol, B. Poudel, A. Nozariasbmarz, W. Li, M. Ibáñez, A. Cabot, *ACS Nano* **2023**, *17*, 8442.

[26] C. Chang, Y. Liu, S. Ho Lee, M. Chiara Spadaro, K. M. Koskela, T. Kleinhanns, T. Costanzo, J. Arbiol, R. L. Brutchey, M. Ibáñez, *Angew. Chem. Int. Ed.* **2022**, *61*, e202207002.

[27] C. Hu, K. Xia, C. Fu, X. B. Zhao, T. Zhu, *Energy Environ. Sci.* **2022**, 15, 1406.

[28] D. An, J. Wang, J. Zhang, X. Zhai, Z. Kang, W. Fan, J. Yan, Y. Liu, L. Lu, C.-L. Jia, M. Wuttig, O. Cojocaru-Mirédin, S. Chen, W. Wang, G. J. Snyder, Y. Yu, *Energy Environ. Sci.* **2021**, *14*, 5469.

[29] L. Xu, Y. Xiao, S. Wang, B. Cui, D. Wu, X. Ding, L.-D. Zhao, *Nat. Commun.* **2022**, *13*, 6449.

[30] Z. Liu, T. Hong, L. Xu, S. Wang, X. Gao, C. Chang, X. Ding, Y. Xiao, L.-D. Zhao, *Interdiscip. Mater.* **2023**, *2*, 161.

[31] C. Coughlan, M. Ibáñez, O. Dobrozhan, A. Singh, A. Cabot, K. M. Ryan, *Chem. Rev.* **2017**, *117*, 5865.

[32] T.-R. Wei, Y. Qin, T. Deng, Q. Song, B. Jiang, R. Liu, P. Qiu, X. Shi, L. Chen, *Sci. China Mater.* **2019**, *62*, 8.

[33] L. I. Berger, *Ternary Diamond-Like Semiconductors*, Springer Science & Business Media, **2012**.

[34] T.-R. Wei, H. Wang, Z. M. Gibbs, C.-F. Wu, G. J. Snyder, J.-F. Li, *J. Mater. Chem. A* **2014**, *2*, 13527.

[35] C. Yang, F. Huang, L. Wu, K. Xu, *J. Phys. D. Appl. Phys.* **2011**, *44*, 295404.

[36] E. J. Skoug, J. D. Cain, P. Majsztrik, M. Kirkham, E. Lara-Curzio, D. T. Morelli, *Sci. Adv. Mater.* **2011**, *3*, 602.

[37] G. García, P. Palacios, A. Cabot, P. Wahnón, *Inorg. Chem.* **2018**, *57*, 7321.

[38] D. T. Do, S. D. Mahanti, *J. Phys. Chem. Solids* **2014**, *75*, 477.

[39] D. Zhang, J. Yang, Q. Jiang, Z. Zhou, X. Li, J. Xin, A. Basit, Y. Ren, X. He, W. Chu, J. Hou, *ACS Appl. Mater. Interfaces* **2017**, *9*, 28558.

[40] L. Bo, Y. Wang, W. Wang, L. Wang, F. Li, M. Zuo, Y. Ma, D. Zhao, *Results Phys.* **2021**, *26*, 104337.

[41] Y. Liu, G. García, S. Ortega, D. Cadavid, P. Palacios, J. Lu, M. Ibáñez, L. Xi, J. De Roo, A. M. López, S. Martí-Sánchez, I. Cabezas, M. de la Mata, Z. Luo, C. Dun, O. Dobrozhan, D. L. Carroll, W. Zhang, J. Martins, M. V. Kovalenko, J. Arbiol, G. Noriega, J. Song, P. Wahnón, A. Cabot, *J. Mater. Chem. A* **2017**, *5*, 2592.

[42] T. Zhou, L. Wang, S. Zheng, M. Hong, T. Fang, P.-P. Bai, S. Chang, W. Cui, X. Shi, H. Zhao, Z.-G. Chen, *Nano Energy* **2018**, *49*, 221.

[43] B. Wang, S. Zheng, Y. Chen, Y. Wu, J. Li, Z. Ji, Y. Mu, Z. Wei, Q. Liang, J. Liang, *J. Phys. Chem. C* **2020**, *124*, 10336.

[44] C.-H. Chang, C.-L. Chen, W.-T. Chiu, Y.-Y. Chen, *Mater. Lett.* **2017**, *186*, 227.

[45] B. Wang, Y. Wang, S. Zheng, S. Liu, J. Li, S. Chang, T. An, W. Sun, Y. Chen, *J. Alloys Compd.* **2019**, *806*, 676.

[46] J.-M. Song, Y. Liu, H.-L. Niu, C.-J. Mao, L.-J. Cheng, S.-Y. Zhang, Y.-H. Shen, *J. Alloys Compd.* **2013**, *581*, 646.

[47] L. D. Partain, R. A. Schneider, L. F. Donaghey, P. S. McLeod, *J. Appl. Phys.* **1985**, *57*, 5056.

[48] A. Moser, O. Yarema, G. Garcia, M. Luisier, F. Longo, E. Billeter, A. Borgschulte, M. Yarema, V. Wood, *Chem. Mater.* **2023**, *35*, 6323.

[49] S. Poulston, P. M. Parlett, P. Stone, M. Bowker, *Surf. Interface Anal.* **1996**, *24*, 811.

[50] Y. Wang, W. Zhou, R. Jia, Y. Yu, B. Zhang, *Angew. chemie Int. Ed.* **2020**, *59*, 5350.

[51] M. Kim, D. Park, J. Kim, *Dalt. Trans.* **2022**, *51*, 10169.

[52] F. Wan, J.-Z. Guo, X.-H. Zhang, J.-P. Zhang, H.-Z. Sun, Q. Yan, D.-X. Han, L. Niu, X.-L. Wu, *ACS Appl. Mater. Interfaces* **2016**, *8*, 7790.

[53] H. Rupp, U. Weser, *Bioinorg. Chem.* **1975**, *5*, 21.

[54] J. Li, L. Li, X. Ma, X. Han, C. Xing, X. Qi, R. He, J. Arbiol, H. Pan, J. Zhao, J. Deng, Y. Zhang, Y. Yang, A. Cabot, *Adv. Sci.* **2023**, 2300841.

[55] L. Bindi, A. Dasgupta, P. Mukherjee, J. Gao, X. Yang, J. A. Jaszczak, *Phys. Rev. Mater.* **2022**, *6*, 115202.

[56] M. Li, Y. Liu, Y. Zhang, X. Han, K. Xiao, M. Nabahat, J. Arbiol, J. Llorca, M. Ibañez, A. Cabot, *ACS Appl. Mater. Interfaces* **2021**, *13*, 51373.

[57] N. Yi, S. Wang, Z. Duan, K. Wang, Q. Song, S. Xiao, *Adv. Mater.* **2017**, *29*, 1701636.

[58] W. Scott, J. R. Kench, *Mater. Res. Bull.* **1973**, *8*, 1257.

[59] S.-J. L. Kang, *Sintering: Densification, Grain Growth, and Microstructure*, Elsevier, Butterworth-Heinemann, Oxford, **2005**.

[60] Y. Liu, Y. Zhang, K. H. Lim, M. Ibáñez, S. Ortega, M. Li, J. David, S. Martí-Sánchez, K. M. Ng, J. Arbiol, M. V. Kovalenko, D. Cadavid, A. Cabot, *ACS Nano* **2018**, *12*, 7174.

[61] G. J. Snyder, A. H. Snyder, M. Wood, R. Gurunathan, B. H. Snyder, C. Niu, *Adv. Mater.* **2020**, *32*, 2001537.

[62] B. Qin, W. He, L.-D. Zhao, *J. Mater.* **2020**, *6*, 671.

[63] B. Wang, S. Zheng, Q. Wang, Z. Li, J. Li, Z. Zhang, Y. Wu, B. Zhu, S. Wang, Y. Chen, L. Chen, Z.-G. Chen, *Nano Energy* **2020**, *71*, 104658.

[64] D. Do, V. Ozolins, S. D. Mahanti, M.-S. Lee, Y. Zhang, C. Wolverton, *J. Phys. Condens. Matter* **2012**, *24*, 415502.

[65] D. T. Do, S. D. Mahanti, *J. Alloys Compd.* **2015**, *625*, 346.

[66] D. Zhang, J. Yang, H. Bai, Y. Luo, B. Wang, S. Hou, Z. Li, S. Wang, *J. Mater. Chem. A* **2019**, *7*, 17648.

[67] D. Zhang, R. Zhong, S. Gao, L. Yang, F. Xu, P. He, G. Liu, X. San, J. Yang, Y. Luo, S. Wang, *Sci. China Mater.* **2023**, *66*, 3644.

[68] H. S. Kim, Z. M. Gibbs, Y. Tang, H. Wang, G. J. Snyder, *APL Mater.* **2015**, *3*, 1.

[69] L. Zhao, L. Yu, J. Yang, M. Wang, H. Shao, J. Wang, Z. Shi, N. Wan, S. Hussain, G. Qiao, J. Xu, *Mater. Chem. Phys.* **2022**, *292*, 126669.

[70] A. Pal, K. Shyam Prasad, K. Gurukrishna, S. Mangavati, P. Poornesh, A. Rao, Y.-C. Chung, Y. K. Kuo, *J. Phys. Chem. Solids* **2023**, *175*, 111197.

[71] D. R. Clarke, *Surf. Coatings Technol.* **2003**, *163–164*, 67.

[72] W. Wang, Y. Wang, L. Bo, L. Wang, F. Li, M. Zuo, D. Zhao, *J. Alloys Compd.* **2021**, *878*, 160358.

[73] D. Zhang, J. Yang, Q. Jiang, Z. Zhou, X. Li, Y. Ren, J. Xin, A. Basit, X. He, W. Chu, J. Hou, *J. Alloys Compd.* **2017**, *724*, 597.

[74] G. G. Kresse, J. J. Furthmüller, *Phys. Rev. B. Condens. Matter* **1996**, *54*, 11169.

[75] J. Furthmüller, J. Hafner, G. Kresse, *Phys. Rev. B* **1996**, *53*, 7334.

[76] G. Kresse, J. Furthmüller, *Comput. Mater. Sci.* **1996**, *6*, 15.

[77] V. Wang, N. Xu, J.-C. Liu, G. Tang, W.-T. Geng, *Comput. Phys. Commun.* **2021**, *267*, 108033.

The table of contents entry should be 50–60 words long and should be written in the present tense. The text should be different from the abstract text.

Shanhong Wan, Shanshan Xiao, Mingquan Li, Xin Wang, Khak Ho Lim, Min Hong,* Maria Ibáñez, Andreu Cabot, Yu Liu,*

Title

Band Engineering through Pb-doping of Nanocrystal Building Blocks to Enhance Thermoelectric Performance in Cu_3SbSe_4

ToC figure

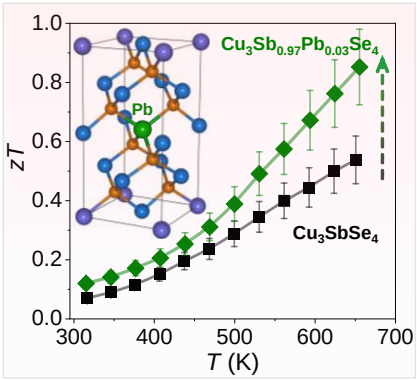

55 mm broad × 50 mm high

This study presents a colloidal synthesis method to produce high-yield Cu_3SbSe_4 NCs. We explore the influence of systematic Pb doping on electrical transport, highlighting the roles of increased p_H and m_d*. Emphasis is given to the lattice distortions caused by the large ionic radii of Pb^{2+} and their implications on the κ_L, and the consequential enhancements in the TE figure of merit zT are detailed.